2014 IEEE/RSJ International Conference on
Intelligent Robots and Systems (IROS 2014)
September 14-18, 2014, Chicago, IL, USA

Design of A Unified Active Locomotion Mechanism for A Wireless Laparoscopic Camera System

Xiaolong Liu[1] and Gregory J. Mancini[2] and Jindong Tan[1]

***Abstract*— This paper proposes an active locomotion mechanism for a wireless laparoscopic surgical camera. The mechanism consists of a stator with 17 iron-core coils and a rotor with 3 cylindrical permanent magnets inside the camera. Our motor-free design unifies the camera's fixation and manipulation by adjusting input currents in the stator which generates 3D rotational magnetic fields, and decouples the camera's locomotion into pan motion and tilt motion. In the simulation studies, our proposed design can conservatively achieve 360° pan motion with a 22.5° resolution, and 127° ~ 164° maximum tilting range for tilt motion which depends on tilt motion working modes and the distance between the rotor and the stator.**

I. INTRODUCTION

Single port access surgery is a popular Minimally Invasive Surgery (MIS) technique, which makes a single small incision or uses a natural orifice in human anatomy to insert surgical instruments and laparoscopic cameras through the incision. The laparoscopic cameras serve as a crucial character that feedbacks visual information to guide surgical procedures. A standard trocar laparoscopic camera is mostly adopted by pushing a long stick through an incision. However, a shared incision limits the dexterity of surgical instruments and the field of views of laparoscopic cameras.

Compared with a conventional insertable laparoscopic camera, a surgical camera system, which can be inserted into patient's anatomy through a natural orifice or an incision and actively controlled for adjusting the camera's visualization target, is more desirable. One of the most important research challenges for such a camera system is the development of locomotion mechanism. There are two key problems for designing the locomotion mechanism: fixation that holds the camera in a stable position and manipulation that actuates the camera to its desired visualization target direction. The state-of-the-art techniques for fixating the inserted cameras are categorized as (i) suturing the cameras against abdominal wall [1], [2] or piercing the cameras into the abdominal wall by needles [3], and (ii) applying external permanent magnets (EPMs) to attract the camera magnetically. The major drawback of a suturing or piercing fixation is not only does this method injure the patient's body but it also leads to poor flexibility for translating the device to a new desired location.

[1]Xiaolong Liu and Jindong Tan are with Department of Mechanical, Aerospace and Biomedical Engineering, University of Tennessee, Knoxville, TN 37996, USA xliu57@utk.edu,tan@utk.edu

[2]Gregory J. Mancini is with Department of Surgery, University of Tennessee, Knoxville, TN 37996, USA GMancini@mc.utmck.edu

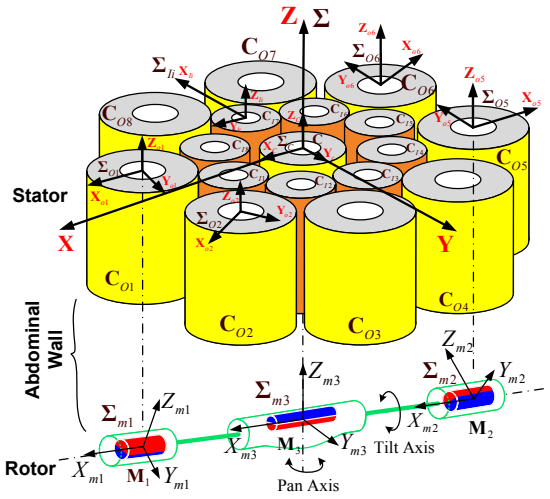

Fig. 1. The conceptual illustration of the our proposed locomotion mechanism design.

Due to the awkward situation of piercing fixation, EPMs tend to address this issue by magnetic links. A ceiling pan/tilt camera which has a cylindrical housing with attached magnets at tail ends is anchored by an EPM to adjust positions and pan angles of the camera [4]. A motor inside generates tilt motions for the camera. A wireless laparoscopic camera with two motor-driven donut-shaped magnets is assisted with an EPM handle for achieving pan and tilt motions [5]. Two modified designs of [5] are proposed in [6], [7].

Research efforts so far have addressed separate mechanisms for locomotion which results in motor involved systems for generating tilt motions. A motor embedded camera requires complex peripheral assisted mechanisms, and relies on the performance of on-board batteries. Some state-of-the-art endoscopic systems have applied magnetic guidance for locomotion of capsule endoscopes. A capsule-shaped endoscopic camera with a permanent magnet inside and a spiral structure outside is actuated by an external rotational magnetic field [8]. By positioning an EPM installed robot end-effector, roll and pitch motions of an endoscopic camera ,which is embedded with four identical axially magnetized cylinder magnets, are achieved for inspecting gastrointestinal (GI) tract [9]. However, the locomotion mechanisms of the endoscopic cameras are not suitable to be used in a laparoscopic camera. Most of the magnetic guidance endoscopic cameras are designed for traveling along GI tract, or being manipulated in fluids. The fixation function is insignificant for the endoscopic cameras. But for laparoscopic cameras,

978-1-4799-6934-0/14/$31.00 ©2014 IEEE

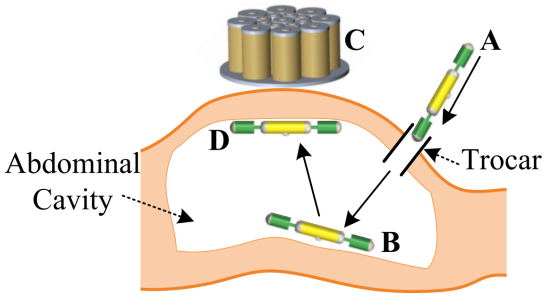

Fig. 2. Application scenario of the laparoscopic camera system.

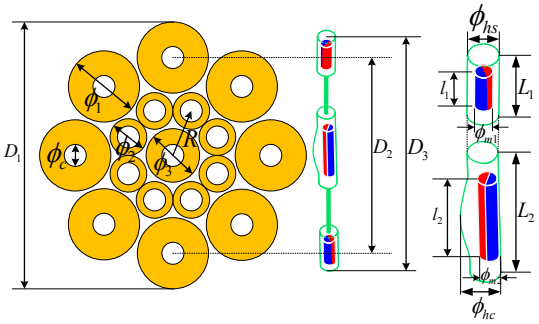

Fig. 3. Rotor and stator design.

the fixation and manipulation have to be cooperatively working all the time in order to keep the camera in position and change the visual direction.

Inspired by spherical actuators [10], [11], [12], we propose a novel motor-free locomotion mechanism design for a wireless laparoscopic camera in this paper. Our design unifies the camera's fixation and manipulation by adjusting input currents of a stator which is independent of on-board power supply. A rotor with permanent magnets inside the camera is magnetically coupled to the stator placed against or close to the dermal surface. The stator generates a 3D rotational magnetic field, decouples the camera's orientation actuation into pan motion and tilt motion, and provides force to serve as an anchoring system that keeps the camera steady during a surgical procedure.

II. CONCEPT AND ROTOR/STATOR DESIGNS OF WIRELESS LAPAROSCOPIC CAMERA SYSTEM

A. Concept of Design

The locomotion mechanism of laparoscopic camera system consists of a magnetic rotor and a coil winding stator. In this paper, we concentrate on developing the locomotion mechanism and leave out the other components in the camera for future work. The camera design has three housings connected by two rigid bars, as shown in Fig. 1. Each of the housing can freely rotate around the axis of the bar. For each tail-end housing, a diametrically magnetized cylindrical magnet is embedded with a free axial rotation relative to its housing. One diametrically magnetized cylindrical magnet is fixed with the central housing. All the other main components of the camera, such as a camera module, batteries, internal sensors, wireless modules, are sealed in the central housing. The stator consists of multiple coils to generate a rotating magnetic field for pan and tilt motions of the camera.

Fig. 2 shows the application scenario of our proposed laparoscopic camera system. To insert the laparoscopic camera (A) into the patient's abdominal cavity, a trocar has to be applied first. After the camera reaches to (B) position, the stator (C) is activated for attracting the camera against the abdominal wall at position (D). The process of posing camera from (B) to (D) can be assisted by using laparoscopic clamp forceps. A surgeon controls the current inputs to adjust a desired camera visual direction.

The working principle of our proposed camera system is illustrated in Fig. 1. The system is designed to enable two types of motions: orientation and translation. The orientation control is decoupled into a pan motion control and a tilt motion control that are capable to function separately based on our design. To initialize the pose of the camera, C_{O1}, C_{O5}, C are activated to align magnets $\mathbf{M}_1$, $\mathbf{M}_2$, $\mathbf{M}_3$ with the coils respectively.

For the pan motion of the camera, outer coils and tail-end magnets $\mathbf{M}_1$, $\mathbf{M}_2$ are mainly involved. Due to the symmetric design of the stator and rotor, the motion, that magnet $\mathbf{M}_1$ rotates from aligning with C_{O1} to aligning with C_{O2} while magnet $\mathbf{M}_2$ rotates from C_{O5} to C_{O6}, is the whole process we need to discuss. In order to keep the camera rotating around pan-axis during the pan motion, the current values in C_{O5} and C_{O6} have to separately synchronized with C_{O1} and C_{O2}. After the camera reaches the desired pan angle, the outer coils will replace the function of central coil C to provide the fixation of the camera against the abdominal wall.

The tilt motion is activated by the remaining coils to generate a torque along X_{m3} axis on the central magnet $\mathbf{M}_3$. The eletromagnetic torque applied on $\mathbf{M}_3$ generate a rotational motion on the central housing around tilt axis due to the fixed attachment of $\mathbf{M}_3$ and its housing. The purpose of translational control is to reposition the camera to a desired location. It can be achieved by the initialized coil setting and moving the stator manually. The magnets follow the repositioning of the stator to a new location.

TABLE I
STATOR AND ROTOR DESIGN, UNIT: [MM]

Stator				Rotor			
ϕ_1	32	R	23	ϕ_{hs}	12	l_1	12.7
ϕ_2	17	D_1	122	ϕ_{hc}	13	l_2	25.4
ϕ_3	24	D_2	90	ϕ_{m1}	6.35	L_1	14
ϕ_c	10	D_3	102	ϕ_{m2}	6.35	L_2	40

B. Stator and Rotor Design

According to the working principle introduced in Section II-A, it is desired to have the stator design with symmetric structure which arranges coils circularly around one central coil. To make the stator have sufficient control capability,

it is designed with 8 outer coils, 8 inner coils, and 1 central coil by considering the compromise between coil sizes and the number of coils, as shown in Fig. 3. The specifications of the rotor and stator design are shown in Table I. All the coils in the stator are 50 mm in height and winded by AWG23 copper wires which can tolerate 2.5 A maximum current. The windings of an outer coil, an inner coil and the central coil are 2000, 600, and 1000 turns respectively. For generating stronger magnetic field compared with air-core stators, iron cores with diameter 9 mm, height of 50 mm are applied to all the coils. Three diametrically magnetized cylindrical magnets are in three separate housings of the camera. Two identical tail-end magnets are with the residual magnetization 1.32 T, and the central magnet is with the residual magnetization 1.43 T.

III. ACTIVE LOCOMOTION MECHANISM MODEL

The objective of building an analytical model for the camera system's locomotion mechanism is twofold: to analyze the locomotion capabilities of the proposed design; and to control of the laparoscopic camera in real time. In this paper, we focus on the first objective based on the analytical model. The central problem of developing the model is how to calculate forces and torques generated on the magnets. The analytical models of spherical motors are based on Lorentz law due to their air-core stators [10], [11], [12]. In our application the thickness of the abdominal wall is much greater than the air gap in the spherical motors. Iron-core coils are thus considered because the high magnetic permeability of soft iron can significantly enhance the coil's magnetic field. However, the Lorentz law can not handle the force and torque analysis with iron-core coils.

An alternative way to formulate magnetic force and torque is to consider a magnet as a magnetic moment $\mathbf{M}$. The equations can be represented as

$$\mathbf{T} = \mathbf{M} \times \mathbf{B}, \quad \mathbf{F} = (\mathbf{M} \cdot \nabla)\mathbf{B}, \tag{1}$$

where $\mathbf{B}$ is the magnetic flux density at the location of $\mathbf{M}$ [13]. If the size of the magnet is small enough, it can be assumed that the magnetic field applied over the magnet is uniform. Under this assumption, the computation of (1) is greatly simplified. However, considering the thickness of an abdominal wall and the sizes of magnets in our camera, it is not appropriate to use the assumption for deriving our analytical model. Therefore, two main problems have to be addressed first: how to represent the magnetic field of the iron-core stator; and how to calculate the magnetic force and torque without the simplified assumption. Then analytical models of the pan and tilt motions are developed.

A. Stator's Magnetic Flux Density $\boldsymbol{B}$

For modeling the stator's magnetic flux density, a set of coordinates have to be set first. As shown in Fig. 1, Σ_{Oi}, Σ_{Ii}, Σ_C are the local frame of outer coils, inner coils and central coil respectively, where $i = 1,...,8$. It is important to note that for the purpose of clear illustration, we draw the coil's local coordinates on the top of them. But in all the following model developments, we set the origins of the local coordinates at the coil's bottoms. The representations of $\mathbf{M}$ and $\mathbf{B}$ in (1) have to share the same coordinates. Therefore, the central coil local frame Σ_C is adopted as a reference frame $\Sigma = \{X, Y, Z\}$ for establishing the relationship of coordinates between the stator and rotor. The transformation from local coil frame Σ_j to the reference frame Σ is expressed as

$$\mathbf{P} = \mathbf{R}_j \mathbf{P}_j + \mathbf{T}_j, \tag{2}$$

where $\mathbf{P} = (x, y, z)$ and $\mathbf{P}_j = (x_j, y_j, z_j)$ are the same point in Σ and Σ_j, and $j = Oi, Ii, C$. $\mathbf{R}_j$ and $\mathbf{T}_j$ are a rotational matrix and a translational vector.

It has been claimed in [14] that an iron-core coil's magnetic flux density has linear relationships with its input current, and all the individual fields can be superimposed linearly. This assumption has been verified at the coinciding point of the axes of the coils. According to our stator design, the working space is not under the verified region. We extend the assumption that it still holds when the working space has an offset to the coil axes. This extended assumption is verified in Section IV-A. The superimposed magnetic flux density in Σ is represented as

$$\mathbf{B}(x, y, z) = \sum_{j=1}^{N} \mathbf{R}_j \mathbf{B}_j^u (x_j, y_j, z_j) I_j, \tag{3}$$

where $\mathbf{B}_j^u$ is the unit current magnetic flux density of coil j in its local frame; N is the number of coils. Finite Element Method (FEM) can yield accurate solutions of a coil's magnetic flux density by building extra fine meshes. However, the expensive computational time of FEM fails this method to serve in a real time application. A magnetic dipole model fitting method proposed in [14], which adopts the coil's axial magnetic flux density from FEM as the fitting data, is applied for estimating the parameter p and $\mathbf{l}$ in

$$\mathbf{B}_j^u(\mathbf{P}_j) = \frac{\mu_0}{4\pi} \left(-\frac{\mathbf{M}}{|\mathbf{P}_j|^3} + \frac{3(\mathbf{M} \cdot \mathbf{P}_j)\mathbf{P}_j}{|\mathbf{P}_j|^5} \right), \tag{4}$$

where $\mathbf{M} = p\mathbf{l}$ is the coil's equivalent magnetic moment.

B. Rotor's Magnetic Moment $\boldsymbol{M}$

To calculate (1), the magnetic moments $\mathbf{M}$ have to be determined. The rotor of the camera consists of three diametrically magnetized cylinder magnets: one central magnet fixed with its housing, two tail-end magnets rotationally free around the tilt axis with respect to their housings. Body fixed frames of the magnets are set as Σ_{m1}, Σ_{m2} and Σ_{m3}. The magnetic moment of the kth magnet in Σ_{mk} is expressed as

$$\mathbf{M}_k = M_0 V \cdot [0, 0, 1]^T, \tag{5}$$

where $k = 1, 2, 3$; M_0 is the residual magnetization of the magnet; $V = \pi(a_k/2)^2 l_k$ is the volume of the magnet k; a_k and l_k are the diameter and length of the kth magnet; The transformation from Σ_{mk} to Σ is represented by

$$\mathbf{P} = \mathbf{R}_{mk} \mathbf{P}_{mk} + \mathbf{T}_{mk}, \tag{6}$$

where $\mathbf{P}_{mk}$ denotes a point in Σ_{mk}. $\mathbf{R}_{mk}$ and $\mathbf{T}_{mk}$ are a rotational matrix and a translational vector.

C. Force and Torque Modeling

The locomotion of the camera depends on forces and torques applied on all the three magnets. A strategy to solve this problem is to calculate the force and torque separately on each magnet and superimpose them. For deriving the magnetic force and torque on magnet $\mathbf{M}_k$, $\mathbf{B}$ has to be integrated over the magnet's volume V. Due to the complexity of $\mathbf{B}$, it is cumbersome to use its exact representation in (3). Instead, expending the magnetic field at the origin point of Σ_{mk} by using Taylor series expansion is an effective way to simplify $\mathbf{B}$ [15]. Equation (1) is reformulated as

$$\bar{\mathbf{T}}_k = \int_V \{(\mathbf{M}_k \times \widetilde{\bar{\mathbf{B}}}) + [\bar{\mathbf{r}} \times (\mathbf{M}_k \cdot \nabla)\widetilde{\bar{\mathbf{B}}}]\}\, dv, \quad (7)$$

$$\bar{\mathbf{F}}_k = \int_V (\mathbf{M}_k \cdot \nabla)\widetilde{\bar{\mathbf{B}}}\, dv, \quad (8)$$

where '-' represents a vector in Σ_{mk}, $\bar{\mathbf{r}}$ is the position of an element of the magnet in Σ_{mk}; $\widetilde{\bar{\mathbf{B}}}$ and $\widetilde{\mathbf{B}}$ are Taylor series expansions of $\mathbf{B}$ in Σ_{mk} and Σ respectively; and $\widetilde{\bar{\mathbf{B}}} = \mathbf{R}_{mk}\widetilde{\mathbf{B}}|_{(\mathbf{P}=\mathbf{R}_{mk}\mathbf{P}_{mk}+\mathbf{T}_{mk})}$. Equations (7) and (8) are solved by ignoring high order gradient terms, i.e.

$$\bar{T}_{k\bar{x}} = -m_k V(\lambda_2^k B_x + \eta_2^k B_y + \zeta_2^k B_z), \quad (9)$$

$$\bar{T}_{k\bar{y}} = m_k V(\lambda_1^k B_x + \eta_1^k B_y + \zeta_1^k B_z), \quad (10)$$

$$\begin{aligned}\bar{T}_{k\bar{z}} =& (1/12)m_k V l_k^2(\lambda_2^k B_{x\bar{z}\bar{x}} + \eta_2^k B_{y\bar{z}\bar{x}} + \zeta_2^k B_{z\bar{z}\bar{x}}) - \\ & (1/4)m_k a_k^2 V(\lambda_1^k B_{x\bar{z}\bar{y}} + \eta_1^k B_{y\bar{z}\bar{y}} + \zeta_1^k B_{z\bar{z}\bar{y}}),\end{aligned} \quad (11)$$

$$\bar{F}_{k\bar{x}} = m_k V(\lambda_1^k B_{x\bar{z}} + \eta_1^k B_{y\bar{z}} + \zeta_1^k B_{z\bar{z}}), \quad (12)$$

$$\bar{F}_{k\bar{y}} = m_k V(\lambda_2^k B_{x\bar{z}} + \eta_2^k B_{y\bar{z}} + \zeta_2^k B_{z\bar{z}}), \quad (13)$$

$$\bar{F}_{k\bar{z}} = m_k V(\lambda_3^k B_{x\bar{z}} + \eta_3^k B_{y\bar{z}} + \zeta_3^k B_{z\bar{z}}), \quad (14)$$

where B_i is ith component of $\mathbf{B}$ in Σ; B_{ij} is the first order gradient of B_i on variable j; B_{ijr} is the second order gradient of B_{ij} on variable r. In (9), (10), $j = x, y, z$ is a coordinate in Σ. In (11)-(14), $j, r = \bar{x}, \bar{y}, \bar{z}$ are coordinates in Σ_{mk}. $\lambda_n^k, \eta_n^k, \zeta_n^k, \rho_n^k$ are the components of $\mathbf{R}_{mk} = (\boldsymbol{\lambda}^k, \boldsymbol{\eta}^k, \boldsymbol{\zeta}^k)_{3\times 3}$ and $\mathbf{T}_{mk} = (\rho_1^k, \rho_2^k, \rho_3^k)^T$, $n = 1, 2, 3$.

Because the number of coils is 17, (7) and (8) are decomposed as a 3×17 force matrix $\bar{\mathbf{F}}_k^u$, a 3×17 torque matrix $\bar{\mathbf{T}}_k^u$ and a 17×1 input current vector $\mathbf{I}$. $\bar{\mathbf{T}}_k^u$ and $\bar{\mathbf{F}}_k^u$ are derived from unit current inputs. Since all the forces and torques should be analyzed in a common frame, $\bar{\mathbf{T}}_k$ and $\bar{\mathbf{F}}_k$ have to be represented in the reference frame by using $\mathbf{R}_{mk}$,

$$\mathbf{T}_k = \mathbf{R}_{mk}\bar{\mathbf{T}}_k^u\mathbf{I}, \quad \mathbf{F}_k = \mathbf{R}_{mk}\bar{\mathbf{F}}_k^u\mathbf{I}. \quad (15)$$

With (15), different groups of coils can be activated to achieve desired motions.

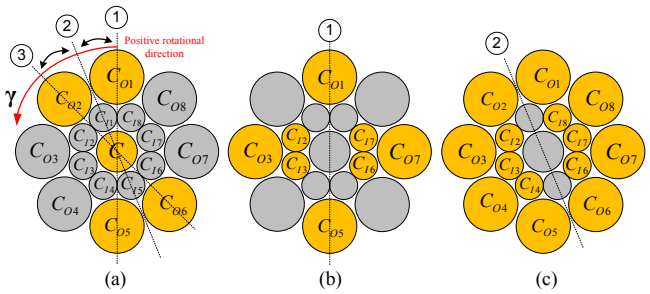

Fig. 4. Pan and tilt motion working modes. (a) illustrates a single phase of pan motion; (b) shows tilt mode 1; and (c) shows tilt mode 2.

D. Pan Motion Analytical Model

The idea of the locomotion mechanism of our proposed camera system is to separately activate its pan and tilt motions. The coil activation of pan motion is shown in Fig. 4(a) where the highlighted circles are the coils to be activated. A full 360° pan motion consists of 8 identical phases. Fig 4(a) shows a single phase of coils activation. The camera is centered at C and rotated from ① to ③ by adjusting the current inputs in $C_{O1,2,5,6}$. During the pan motion, the currents in C_{O5} and C_{O6} is simultaneous with C_{O1} and C_{O2} respectively while coil C provides attractive force for the camera fixation. Theoretically, the camera can stop at any pan angle between ① and ③ by adjusting the input currents. But in practical applications, a 22.5° resolution is sufficient because field of views (FOV) of commercially available camera modules are much larger than 22.5°, e.g. PillCam SB2 (Given Imaging Inc.) with FOV 156°, MicroCam (IntroMedic Inc.) with FOV 150° [16].

Due to the symmetrical structure of the camera system, only $\mathbf{M}_1$ is analyzed under coil C_{O1} and C_{O2}. To calculate the force and torque, $\mathbf{M}_1$'s direction has to be determined according to (5) and (6). Considering $\mathbf{M}_1$ aligns with the magnetic field generated by $C_{O1,2}$, the currents are designed with the rotational feedback angle γ around $\mathbf{Z}$ axis, as shown in Fig. 4(a). For the pan motion from position ① to ②, the currents are designed as

$$I_{O1} = \begin{cases} \xi I_{max} + (1-\xi)I_{max}(1 - \left|\frac{\gamma-\gamma_{g1}}{\gamma_{g1}}\right|), \gamma < \gamma_{g1} \\ I_{max}, \gamma \geq \gamma_{g1} \end{cases} \quad (16)$$

$$I_{O2} = \begin{cases} I_{max}, \gamma < \gamma_{g1}, \\ \xi I_{max} + (1-\xi)I_{max}(1 - \left|\frac{\gamma-\gamma_{g1}}{\gamma_{g1}}\right|), \gamma \geq \gamma_{g1} \end{cases} \quad (17)$$

where $\xi \in [0, 1]$ is a coefficient, which initially reduces I_{O1} for the starting of the rotation; $|I_{max}| \leq 2.5$ A; $\gamma_{g1} = 22.5°$. To rotate the camera from ② to ③, $C_{O1,2}$ are activated by setting $I_{O1} = 0$,

$$I_{O2} = \xi I_{max} + (1-\xi)I_{max}\left|(\gamma - \gamma_{g2})/\gamma_{g2}\right|, \quad (18)$$

where $\gamma_{g2} = 45°$. The direction of magnetic field generated by $C_{O1,2}$ at the center of $\mathbf{M}_1$ in Σ_{m1} is represented as

$$\mathbf{d}_1 = \mathbf{R}_{m1}^T \frac{\mathbf{R}_{O1}\mathbf{B}_{O1}^u I_{O1} + \mathbf{R}_{O2}\mathbf{B}_{O2}^u I_{O2}}{|\mathbf{R}_{O1}\mathbf{B}_{O1}^u I_{O1} + \mathbf{R}_{O2}\mathbf{B}_{O2}^u I_{O2}|}. \quad (19)$$

Therefore, the forces applied on $\mathbf{M}_{1,2,3}$ are derived according to (15)

$$\mathbf{F}_k = \mathbf{R}_{mk}\bar{\mathbf{F}}_k^u \mathbf{I}_k^{act}, \tag{20}$$

$\mathbf{I}_k^{act}$ is the current vector of activated coils, $k = 1,2,3$.

Fig. 5 illustrates the dynamics of the camera system which is analyzed in Σ_o. $\mathbf{X}_o$ is along the camera's long axis, $\mathbf{Z}_o$ is with the same direction of $\mathbf{Z}$ in Σ, and $\mathbf{Y}_o$ is perpendicular to $\mathbf{X}_o$ and $\mathbf{Z}_o$. $F_1^{x,y,z}$ and $F_2^{x,y,z}$ are derived by using $\mathbf{F}_1$, $\mathbf{F}_2$ and the camera's pan angle with respect to Σ. The magnetic torques T_1^m and T_2^m rotate the tail-end magnets to align with the magnetic field. Due to the lubricated friction between the tail-end magnet and its housing, we only need to confirm that T_1^m and T_2^m can overcome T_f^{m1} and T_f^{m2} when the tail-end housings are moving.

$$T_i^m \geq T_f^{mi} = \mu_{lub}|\mathbf{F}_i^y + \mathbf{F}_i^z|r_{mag}, \tag{21}$$

where T_f^{mi} is the frictional torque between the magnet and its housing; μ_{lub} is the lubricated friction coefficient; r_{mag} is the radius of the magnet; and F_i^z is the magnetic force in $\mathbf{Z}_o$ direction, $i = 1,2$. (21) will be validated in Section IV-D.

The pan motion is actuated by F_1^y and F_2^y. By considering the tissue-housing sliding friction coefficient μ_{tis} as 0.1 [17], the lubricated friction coefficient μ_{lub} between metal and plastic can be made smaller than μ_{tis}. The tail-end housings roll against the tissue if (22) is satisfied

$$T_{pan=}r_{cam}(F_1^y + F_2^y - F_1^r - F_2^r) - T_f^{pan} \geq 0, \tag{22}$$

where $r_{cam} = D_2/2$; $F_{1,2}^r$ are the rolling resistances between the housings and the tissue; T_f^{pan} is the central housing's spinning frictional torque which is modeled by

$$T_f^{pan} = \mu_{tis}(F_1^z + F_2^z + F_3^z - G)r_{avg}, \tag{23}$$

where $r_{avg} = L_2/4$ is the average distance from the rotational center to friction applied point on the central housing; G is the whole gravity of the camera. To fix the camera against the abdominal wall,

$$F^z = F_1^z + F_2^z + F_3^z - G > 0, \tag{24}$$

has to be always satisfied. The rolling resistance $F_{1,2}^r$ are modeled by following Hunter's work [18], which is under some assumptions: the tissue is a viscoelastic half space by comparing thickness of abdominal wall (30 $\sim$ 50 mm) and tail-end housing indention (maximum indention is $\phi_{hs}/4$ = 6 mm) and the tail-end housing rotates at constant velocity V which neglects the acceleration term in order to simplify the preliminary analysis.

$$F_i^r = \frac{2F_N}{\phi_{hs}}(b - \frac{V\tau}{1+f} + \Gamma\frac{a_0}{a}), \tag{25}$$

where F_N is the load per unit length of a cylindrical tail-end housing; τ and f are parameters which specify the model of the viscoelastic tissue; a_0 denotes semicontact width of the housing when $V = 0$. The unknown variables a, Γ, b are solved by a set of boundary conditions.

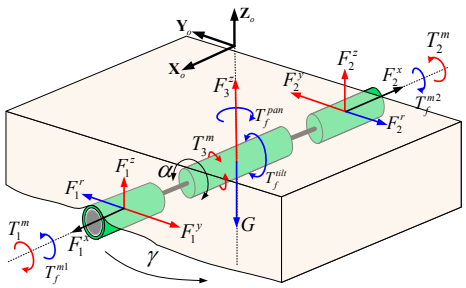

Fig. 5. Analysis of the camera system dynamics.

E. Tilt Motion Analytical Model

In tilt motion modes, the central coil C is set off and replaced by the outer coils to provide attractive force for pulling the camera against the abdominal wall. As shown in Fig. 4(b) and 4(c), the dash lines represent the two tilt modes. In Fig. 4(b), coil $C_{O1,5}$ are activated for balancing the weight of the camera, and coil $C_{I2,3,6,7}$, $C_{O3,7}$ are activated for generating tilt motions on the central magnet. Fig. 4(c) is similar to Fig. 4(b), but with coils $C_{O1,2,5,6}$ activated for camera weight balancing and with coils $C_{I2,3,4,6,7,8}$, $C_{O3,4,7,8}$ activated for generating tilt motion. The torque generated by the activated coils are represented by

$$\mathbf{T}_3 = \mathbf{R}_{m3}\bar{\mathbf{T}}_3^u \mathbf{I}_{tilt}, \tag{26}$$

where $\mathbf{I}_{tilt}$ is the current vector of the activated coils. Fig. 4 shows T_3^m is the eletromagnetic rotational torque around the central housing's long axis, and is derived from $\mathbf{T}_3$ by using $\mathbf{R}_{m3}$. The tilt motion of the central housing requires T_3^m can overcome the frictional torque T_f^{tilt} and the torque T_g from central housing 's gravity $\mathbf{G}_c$. Therefore,

$$T_{tilt} = T_3^m - T_f^{tilt} - T_g > 0, \tag{27}$$

has to be satisfied, where T_f^{tilt} is calculated by

$$T_f^{tilt} = \mu_{tis}(F_1^z + F_2^z + F_3^z - G)r_{mag}. \tag{28}$$

The necessary conditions for enabling pan and tilt motions in (21), (22), (24), (27) are validated in Section IV-E.

IV. SIMULATION RESULTS

In this section, the locomotion mechanism of our proposed design is evaluated by simulations. The extended assumption on superimposing magnetic field is firstly verified. The analytical model of magnetic field and electromagnetic force and torque are evaluated by using a benchmark software. And the locomotion capabilities of pan and tilt motions are investigated separately in the last parts.

A. Verification of Extended Assumption

To verify the extended assumption for developing (3), two points in the working space are selected. The evaluation point of pan motion is set on the intersection line of two planes which are a tangent plane to separate coil C_{O1} and C_{O2}, and a cut-through plane which is determined by the two coils' axes, as shown in Fig.6(a) point A. The distance from A

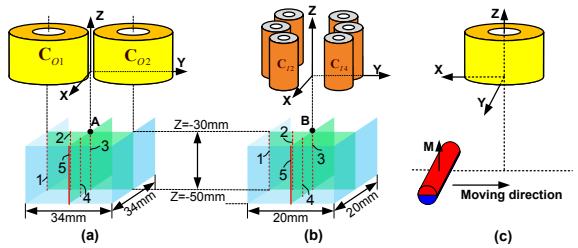

Fig. 6. (a) and (b) illustrate the working space for verifying the extended assumption in Section IV-A, and the evaluation space of the analytical magnetic field in Section IV-B. (c) shows the configuration for evaluating the analytical model of force and torque in Section IV-C.

to the two coils' bottom is set as 30 mm. The tilt motion evaluation point B shown in Fig. 6(b) is set on the axis of the central coil with a distance of 30 mm to the coil's bottom. Coil C_{I2} and C_{I4} are selected for verifying the tilt case. Fig. 7(a) and Fig. 7(b) show the verification results by using COMSOL Multiphysics 4.3a (COMSOL Inc., Sweden). The relative permeability of the iron core is set as 3000 H/m. Fig. 7(a) and 7(b) validate that the magnetic fields generated by the two pairs of coils can be represented by summation of the fields from the individual coils of each pair.

B. Evaluation of the Superimposed Magnetic Fields

For evaluating the superimposed magnetic field in (3), a comparison between the analytical model and the simulation result from COMSOL is implemented. In Fig. 6, two cubic working spaces are selected which are below two outer coils Fig. 6(a) and six inner coils Fig. 6(b) with $Z = -30\,\text{mm} \sim -50\,\text{mm}$. The unit current parameters m and l of an outer coil and an inner coil are $m = 3.81\,\text{Am}^2$, $l = 1.29\,\text{m}$ and $m = 2.41\,\text{Am}^2$, $l = 0.04\,\text{m}$ respectively. Due to the difficulty for analyzing all the points in the working spaces, lines $1-5$ in Fig. 6(a) and lines $1-5$ in Fig. 6(b) are selected according to their representative positions and the symmetry of the working spaces. In Fig. 6(a), (x,y) coordinates of line 1-5 are (0, −17), (0,−11), (0,0), (11,0), (17,0). In Fig. 6(b), (x,y) coordinates of line 1-5 are (0, −10), (0,−5), (0,0), (5,0), (10,0), unit [mm]. The magnetic flux density $\mathbf{B}$ in (3) is expressed by the norm of magnetic field strength $\mathbf{H}$ because of its concise and comprehensive expression of magnetic field. Fig. 8(a) and 8(b) show the comparison between the COMSOL results and our analytical model results for the two working spaces. The average differences are 8.97% (the case in Fig. 6(a)) and 11.86%(the case in Fig. 6(b)).

C. Evaluation of Force and Torque Model

This evaluation aims at proving the validation of the analytical model of force and torque developed in (15). The evaluation is implemented by using diametrically magnetized cylindrical magnets with the two different sizes which have been explained in Section II-B. The long axis of the magnet is perpendicular to XZ plane and centered at X=−20 ∼ 20 mm, Z=−30 mm, as shown in Fig. 6(c). The magnetized direction of the magnet is always kept in $\mathbf{Z}$ direction. The magnetic field is generated by a single coil which

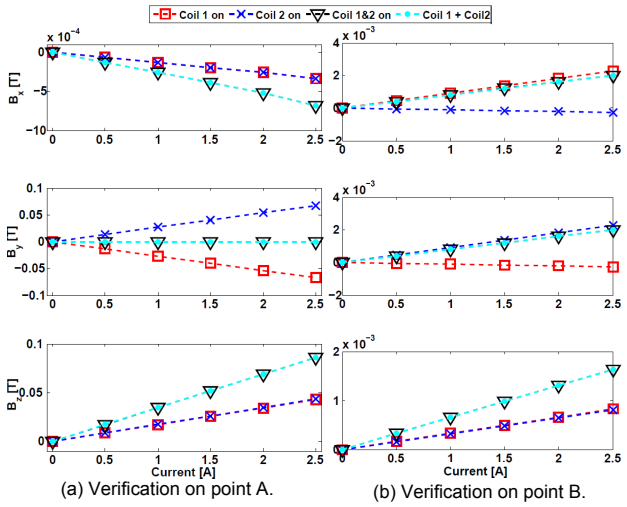

Fig. 7. Verifications on the assumption of superimposing magnetic fields.

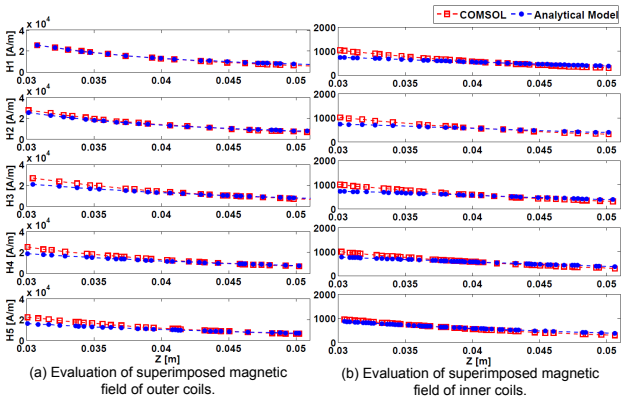

Fig. 8. The analytical model of magnetic field evaluation.

has the configuration of outer coils in Section II-B with a maximum 2.5 A current input. A comparison model is built by COMSOL with 879,160 mesh elements and 1 mm maximum element size of the selected mesh. Fig. 9 shows the comparison results of the force and torque agree well for the magnet with the length of 12.7 mm. For the magnet with the length of 25.4 mm, the agreement of results are worse than the shorter magnet's. This is due to the high order terms in (9)-(14) are ignored in order to simplify the calculation. Although the accuracy of the model can be further improved, it still can provide us a reasonable assessment for the locomotion performance of our proposed design. The following pan/tilt motion analyses will base on this analytical model.

D. Pan Motion Evaluation

In this paper, we conduct qusi-static evaluations to quantize the locomotion capability of the camera system. For the pan motion, (22) and (24) are to be validated by orientating the camera from ① to ③ as shown in Fig. 4(a). The viscoelastic tissue is modeled as Standard Linear Solid (SLS) model which is characterized by spring module $E_1 = 4.28 \times 10^3\ \text{N/m}^2$, spring-dashpot series $E_2 = 1.61 \times 10^4\ \text{N/m}^2$,

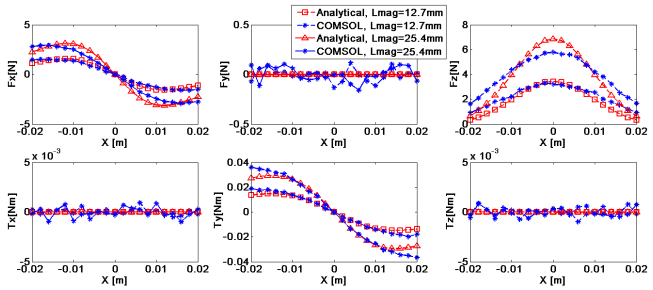

Fig. 9. Analytical force and torque models evaluation on two different sizes of cylindrical magnets.

$\eta = 8.05 \times 10^3$ N-s/m^2, Poisson ratio $\nu = 0.5$ [19]. The friction coefficients are set as $\mu_{tis} = 0.1$, $\mu_{lub} = 0.05$. According to [18], we maximize F_i^r in (25) by setting $V = a_0/\tau$.

The pan motion consists of two phases $0° \sim 22.5°$ and $22.5° \sim 45°$. $C_{O1,2,5,6}$ and C are activated in Fig. 10(d)-10(h). During the period $0° \sim 22.5°$, the currents are set as $I_{O1} = I_{O5}$ (refer to (16)), $I_{O2} = I_{O6} = I_{max}$, $I_C = 0.2$ A with $\xi = 0$, $I_{max} = 2$ A; during the period $22.5° \sim 45°$, the currents are set as $I_{O1} = I_{O5} = 0$, $I_{O2} = I_{O6}$ (refer to (18)), $I_C = 0.2$ A with $\xi = 0.3$, $I_{max} = 2$ A. Fig. 10(a) shows under the distance from the camera to the stator $Z = -35 \sim -50$ mm, T_{pan} is validated until γ reaches to 0.74 rad. The unreached angles can be achieved by the next set coils. Fig. 10(b) validates (24) that the eletromagnetic force in $\mathbf{Z}$ direction can always balance the weight of the camera (assume $G = 30$ grams). Fig. 10(c) validates (21) which shows magnetic torque T_i^m on tail-end magnet can overcome the lubricated frictional torque T_f^{mi} between the magnet and its housing.

E. Tilt Motion Evaluation

The objective of evaluating tilt motion is to analyze the available tilting range constrained by (27) and (24). The tilt motion has two modes as shown in Fig. 4(b) and (c). The central housing is positioned from $\alpha = 0°$ (the magnet is in $\mathbf{Z}$ direction in Σ) to $\alpha = 90°$ (the central housing counterclockwise rotating around the camera shaft). Each mode is investigated by $Z = -35 \sim -50$ mm. The current setting for this evaluation is shown in Table II. Fig.11(a) and 11(d) illustrate when $Z = -35$ mm, 1.37 rad (78.5°) tilt motion for mode 1 and 1.43 rad (82°) tilt motion for mode 2 are available; and when $Z = -50$ mm, 1.14 rad (65.3°) tilt motion for mode 1 and 1.11 rad (63.6°) for mode 2 are available. The full ranges of tilt motion of mode 1 and mode 2 thus vary from 130.6° to 157° and from 127.2° to 164° respectively. Fig. 11(b) and 11(e) validate (24) with a minimum 0.2 N remaining force after balancing the weight of the camera.

The electromagnetic forces for generating tilt motions cause the tail-end magnets a $\mathbf{Y}_0$ direction (as shown in Fig. 5) motion trend by F_f^y. Therefore, it is necessary to compare F_f^y and the sliding friction F_m^y between the camera housings and abdominal wall. Fig. 11(c) and 11(f) show F_f^y is capable to balance F_m^y for keeping the camera in position.

V. CONCLUSIONS AND FUTURE WORK

This paper proposes a novel locomotion mechanism design for a wireless laparoscopic camera. This motor-free design unifies the camera's fixation and manipulation, and enables a decoupled pan and tilt activation of the camera by varying the input current of stator's coils. According to our simulation results, the laparoscopic camera conservatively has the capability to achieve 360° pan motion with a 22.5° resolution, and the range of $127° \sim 164°$ tilt motion which depends on tilt motion working modes and the distance between the camera and the stator.

To control the locomotion of the camera system, the position and orientation feedbacks are necessary. In our future work, the feedback will be built based on camera's vision tracking and magnetic localization by external magnet sensors. The other components of the laparoscopic camera such

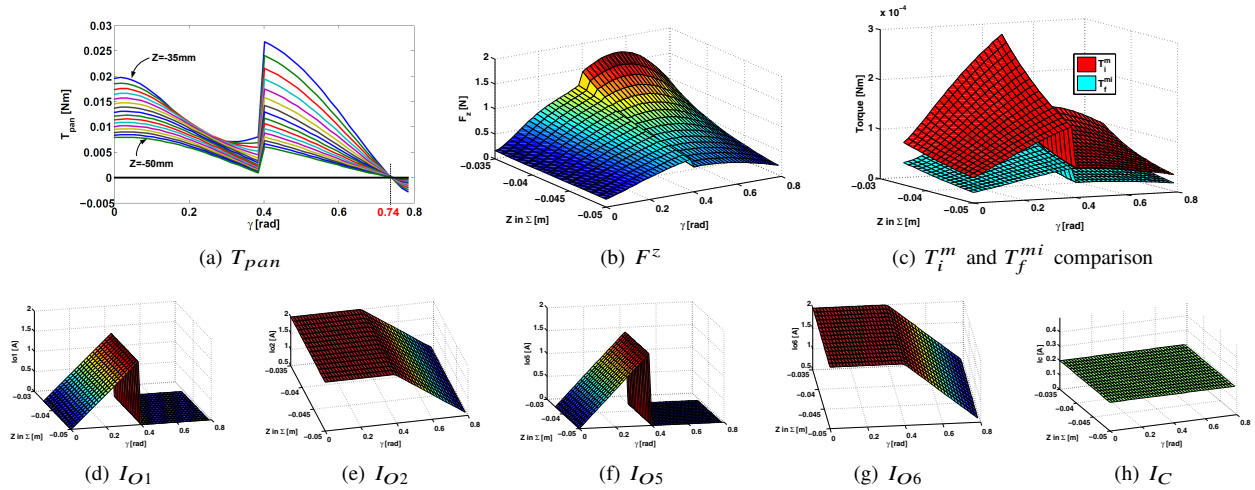

(a) T_{pan} (b) F^z (c) T_i^m and T_f^{mi} comparison

(d) I_{O1} (e) I_{O2} (f) I_{O5} (g) I_{O6} (h) I_C

Fig. 10. Evaluation of pan motion. (a)-(c) validate the necessary conditions in equations (21), (22), (24) for generating a pan motion. (d)-(h) show the activated coils and input current values.

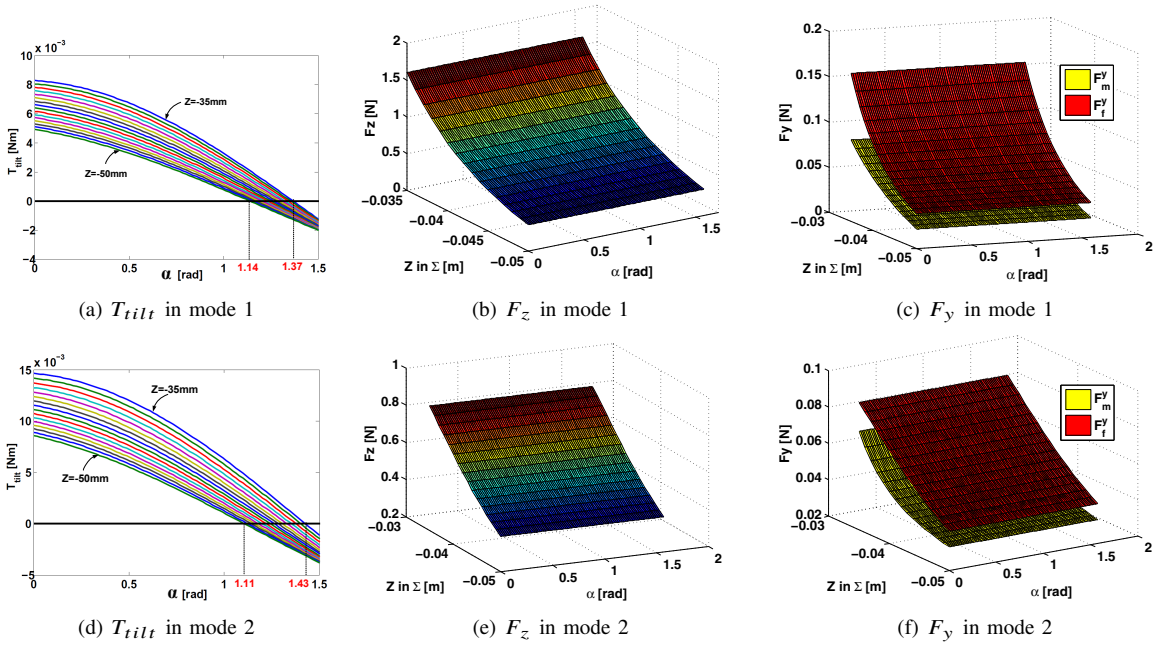

(a) T_{tilt} in mode 1 (b) F_z in mode 1 (c) F_y in mode 1

(d) T_{tilt} in mode 2 (e) F_z in mode 2 (f) F_y in mode 2

Fig. 11. Evaluations of tilt motion. (a)-(c) analyze tilt mode 1, and (d)-(f) analyze tilt mode 2.

TABLE II

INPUT CURRENTS FOR EVALUATING TILT MODE 1 AND MODE 2, UNIT [A]

	I_{O1}	I_{O2}	I_{O3}	I_{O4}	I_{O5}	I_{O6}	I_{O7}	I_{O8}	I_{I1}	I_{I2}	I_{I3}	I_{I4}	I_{I5}	I_{I6}	I_{I7}	I_{I8}	I_C
Mode 1	1	0	−1	0	1	0	1	0	−2.5	−2.5	−2.5	−2.5	2.5	2.5	2.5	2.5	0
Mode 2	1	1	−1	−1	1	1	1	1	0	−2.5	−2.5	−2.5	0	2.5	2.5	2.5	0

as a camera module, batteries, a wireless module, inertial sensors will be designed and fabricated in the laparoscopic camera. For manipulating the camera in a surgical situation, a closed loop controller will be developed for the camera system to enable robust and accurate locomotion controls.

REFERENCES

[1] T. Hu, K. Allen, and L. Fowler, "In-vivo pan/tilt endoscope with integrated light source," in *2007 IEEE/RSJ International Conference on Intelligent Robots and Systems*, pp. 1284 –1289, 2007.

[2] T. Hu, K. Allen, J. Hogle, and L. Fowler, "Insertable surgical imaging device with pan, tilt, zoom, and lighting," *2008 IEEE International Conference on Robotics and Automation*, pp. 2948–2953, 2008.

[3] C. Castro, S. Smith, A. Alqassis, T. ketterl, S. Yu, S. Ross, A. Rosemurgy, P. Savage, and R. Gitlin, "A wireless robot for networked laparoscopy," *Biomedical Engineering, IEEE Transactions on*, vol. 60, no. 4, pp. 930–936, 2013.

[4] S. Platt, J. Hawks, and M. Rentschler, "Vision and task assistance using modular wireless in vivo surgical robots," *Biomedical Engineering, IEEE Transactions on*, vol. 56, no. 6, pp. 1700 –1710, 2009.

[5] P. Valdastri, C. Quaglia, E. Buselli, A. Arezzo, N. D. Lorenzo, M. Morino, A. Menciassi, and P. Dario, "A magnetic internal mechanism for precise orientation of the camera in wireless endoluminal applications.," *Endoscopy*, vol. 42, no. 6, pp. 481–6, 2010.

[6] M. Simi, M. Silvestri, C. Cavallotti, M. Vatteroni, P. Valdastri, A. Menciassi, and P. Dario, "Magnetically activated stereoscopic vision system for laparoendoscopic single-site surgery," *Mechatronics, IEEE/ASME Transactions on*, vol. 18, no. 3, pp. 1140–1151, 2013.

[7] M. Simi, G. Sardi, P. Valdastri, A. Menciassi, and P. Dario, "Magnetic Levitation camera robot for endoscopic surgery," *2011 IEEE International Conference on Robotics and Automation*, pp. 5279–5284, 2007.

[8] M. Sendoh, K. Ishiyama, and K.-I. Arai, "Fabrication of magnetic actuator for use in a capsule endoscope," *Magnetics, IEEE Transactions on*, vol. 39, pp. 3232–3234, Sept 2003.

[9] G. Ciuti, P. Valdastr, A. Menciassi, and P. Dario, "Robotic magnetic steering and locomotion of capsule endoscope for diagnostic and surgical endoluminal procedures," *Robotica*, vol. 28, no. 2, pp. 199–207, 2010.

[10] L. Rossini, O. Chetelat, E. Onillon, and Y. Perriard, "Force and torque analytical models of a reaction sphere actuator based on spherical harmonic rotation and decomposition," *Mechatronics, IEEE/ASME Transactions on*, vol. 18, no. 3, pp. 1006–1018, 2013.

[11] W. Wang, J. Wang, G. Jewell, and D. Howe, "Design and control of a novel spherical permanent magnet actuator with three degrees of freedom," *Mechatronics, IEEE/ASME Transactions on*, vol. 8, no. 4, pp. 457–468, 2003.

[12] Y. Liang, C. I-Ming, Y. Guilin, and L. Kok-Meng, "Analytical and experimental investigation on the magnetic field and torque of a permanent magnet spherical actuator," *Mechatronics, IEEE/ASME Transactions on*, vol. 11, no. 4, pp. 409–419, 2006.

[13] J. D. Jackson, *Classical electrodynamics*. New York, NY: Wiley, 1999.

[14] M. Kummer, J. Abbott, B. Kratochvil, R. Borer, A. Sengul, and B. Nelson, "Octomag: An electromagnetic system for 5-dof wireless micromanipulation," *Robotics, IEEE Transactions on*, vol. 26, no. 6, pp. 1006–1017, 2010.

[15] N. Groom, "Expanded equations for torque and force on a cylindrical permanent magnet core in a large-gap magnetic suspension system," 1997.

[16] A. Moglia, A. Menciassi, P. Dario, and A. Cuschieri, "Capsule endoscopy: progress update and challenges ahead," *Nat Rev Gastroenterol Hepatol*, vol. 6, no. 6, pp. 353–362, 2009.

[17] S. Loring, R. Brown, A. Gouldstone, and J. Butler, "Lubrication regimes in mesothelial sliding.," *Journal of Biomechanics*, vol. 38, no. 12, pp. 2390–6, 2005.

[18] S. Hunter, "The rolling contact of a rigid cylinder with a viscoelastic half space," *Journal of Applied Mechanics*, vol. 28, no. 4, pp. 611–617, 1961.

[19] X. Wang, L. Sliker, H. Qi, and M. Rentschler, "A quasi-static model of wheeltissue interaction for surgical robotics," *Medical Engineering and Physics*, vol. 35, no. 9, pp. 1368 – 1376, 2013.